Excess Thermopower and the Theory of Thermopower Waves

Joel T. Abrahamson,[†] Bernat Sempere,[†,§] Michael P. Walsh,[†] Jared M. Forman,[†,‡] Fatih Şen,[†,⊥] Selda Şen,[†,∥] Sayalee G. Mahajan,[†] Geraldine L. C. Paulus,[†] Qing Hua Wang,[†] Wonjoon Choi,[†] and Michael S. Strano[†,*]

[†]Department of Chemical Engineering and [‡]Department of Chemistry, Massachusetts Institute of Technology, Cambridge, Massachusetts 02139, United States, [§]Instituto Químico de Sarriá, Universitat Ramon Llull, Barcelona 08022, Spain, [⊥]Department of Chemistry, Dumlupinar University, Kutahya 43020, Turkey, and [∥]Department of Chemistry, Middle East Technical University, Ankara, Turkey

ABSTRACT

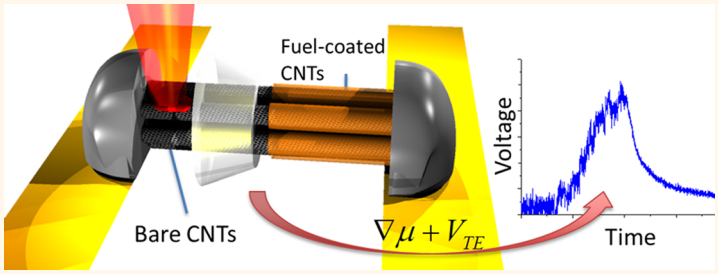

Self-propagating exothermic chemical reactions can generate electrical pulses when guided along a conductive conduit such as a carbon nanotube. However, these thermopower waves are not described by an existing theory to explain the origin of power generation or why its magnitude exceeds the predictions of the Seebeck effect. In this work, we present a quantitative theory that describes the electrical dynamics of thermopower waves, showing that they produce an excess thermopower additive to the Seebeck prediction. Using synchronized, high-speed thermal, voltage, and wave velocity measurements, we link the additional power to the chemical potential gradient created by chemical reaction (up to 100 mV for picramide and sodium azide on carbon nanotubes). This theory accounts for the waves' unipolar voltage, their ability to propagate on good thermal conductors, and their high power, which is up to 120% larger than conventional thermopower from a fiber of all-semiconducting SWNTs. These results underscore the potential to exceed conventional figures of merit for thermoelectricity and allow us to bound the maximum power and efficiency attainable for such systems.

KEYWORDS: thermopower waves · carbon nanotubes · thermoelectric · chemical potential · electronic doping · energy storage

Thermopower waves are promising as new electrical generators at many scales. They allow high-density power generation from chemical fuels.[1,2] Recent measurements show that their power density approaches that of supercapacitors,[3−5] with energy densities in excess of supercapacitors or electrochemical batteries. They also have the advantage of stable and indefinite energy storage.

Thermopower waves generate voltage from a rapidly moving thermal gradient created by an exothermic chemical reaction along a thermally and electrically conductive conduit. Figure 1 depicts the wave on a carbon nanotube (CNT) fiber as an example conduit; MnO_2 films[6] and Sb_2Te_3-coated CNTs[7] have also been demonstrated as conduits recently. The thermal conductivity is higher through the conduit than through the fuel, so forward conduction ahead of the reaction front accelerates the reaction. The thermal wave in turn drives electrical carriers in the same direction, generating an electical power pulse.

However, the electrical properties of such waves are not predicted by the conventional thermoelectric effect and Seebeck coefficient, Γ, defined as the voltage generated per (steady-state) temperature difference. For example, rapid waves initiated at one end of a macrostructure (*e.g.*, an array, fiber, or yarn) of carbon nanotubes typically induce a single-polarity voltage and current pulse.

With obvious cooling behind the wavefront, however, conventional thermoelectric theory predicts a second pulse of opposite sign as the wave reaches the other end and the gradient reverses; the front is the region of highest temperature. Also, the

* Address correspondence to strano@mit.edu.

Received for review November 2, 2012 and accepted July 26, 2013.

Published online July 27, 2013
10.1021/nn402411k

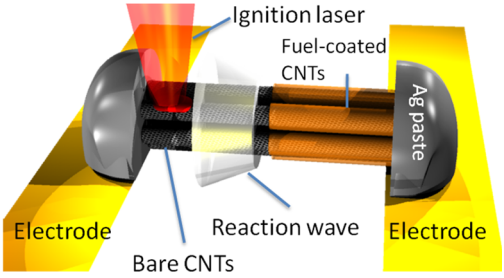

Figure 1. Schematic of thermopower wave generator (TWG). A solid fuel coats the thermal and electrical conduits (prototypically carbon nanotubes [CNTs]), which are connected to electrodes with silver paste. The fuel reacts in a self-propagating thermopower wave when ignited (*via* laser here), which produces an electrical pulse.

magnitude of the voltage peak greatly exceeds the predictions of conventional thermopower in many cases. Consider that thermopower wave generators (TWGs) generated up to 220 mV pulses using cyclotrimethylene trinitramine on aligned multiwalled carbon nanotube (MWNTs) conduits,[1] while the average Seebeck coefficient between 300 and 1400 K is only -10 μV/K for aligned MWNTs,[8] predicting a peak voltage of only 11 mV. Even a more conventional thermoelectric material, thin-film Bi_2Te_3 ($\Gamma \sim 300$ μV/K), generates 150 mV when nitrocellulose reacts at ~600 K in thermopower waves, compared to the Seebeck prediction of 90 mV.[9] Likewise, thermopower waves from nitrocellulose on ZnO produce up to 500 mV, compared with a Seebeck prediction of 155 mV (see Supporting Information for calculation details).[10] Finally, thermopower waves exhibit voltage oscillations with frequency spectra closely matching those of wave velocity oscillations modeled by thermal transport equations.[9,11] The theory of such waves for the description of the electrical pulse is lacking, although the velocity and dynamics of the thermal wave are better understood.[12,13]

Despite their large thermal conductivities, individual SWNTs have practical Seebeck coefficients at room temperature of 40 μV/K.[8,14] In macrostructures, loose contacts between individual nanotubes and bundles can affect the Seebeck coefficient;[8] hence, junction resistance appears important. In individual SWNTs, phonon drag effects are important to thermoelectricity,[15,16] beyond carrier diffusion processes alone. Quantum-confined materials such as nanotubes enhance phonon drag by aligning the motion of phonons and charge carriers, so phonon momentum can be efficiently transferred to charge carriers.[17,18]

Thermopower in carbon nanotubes is environmentally sensitive; the sign of the Seebeck coefficient can reverse when nanotubes are depressurized or thermally annealed. This effect has been attributed to the removal of preadsorbed oxygen, which p-dopes SWNTs.[19,20] Other adsorbed molecules, particularly aromatic hydrocarbons, can shift the Seebeck coefficient of SWNTs by as much as 8 μV/K with only monolayer coverage.[21] Sumanasekera *et al.* say the adsorbates create a new scattering channel for carriers. It is well-known that carriers in SWNTs can couple strongly to π states in adsorbed molecules, enhancing their effects. This system had lower overall $|\Gamma|$ (<10 μV/K) compared to later measurements of SWNTs,[14,22] likely due to the initial vacuum conditions.

In this work, we explore high-speed, synchronized measurement of temperature, voltage, and wave velocity measurements to explore and inform the energy generation mechanism of thermopower waves. These insights lead to a theory of excess thermopower and the first quantitative theory of thermopower wave electrical generation.

RESULTS AND DISCUSSION

Theory of Excess Voltage and Thermopower. A continuum description of the thermoelectric effect within the relaxation time approximation begins with the drift-diffusion equation as the solution to the Boltzmann transport formalism describing carrier motion.[23]

$$J = -\sigma_h\left(E + \frac{\nabla\mu}{e}\right) - L_{12}\nabla T \qquad (1)$$

Here, J is current density, σ_h is electrical conductivity, E is electric field, μ is chemical potential, e is the elementary charge, L_{12} is an Onsager coupling coefficient, and T is temperature. We are interested in holes as the majority carrier, as is the case for p-doped semiconducting (s-) SWNTs at ambient conditions.[14,22,24] Here, we have neglected the tensor form due to the large aspect ratio (>10) of the system. In the limit of zero current, one can solve for E and integrate between two contacts at x_L and x_R to obtain the potential.

$$V = -\int_{x_L}^{x_R} \frac{\nabla\mu}{e} - \frac{L_{12}}{\sigma_h}\nabla T\,dx \qquad (2)$$

Chemical potential is seldom measured separately from electrical potential ($E + \mu/e$), so the Seebeck coefficient is defined as $\Gamma = (E + \nabla\mu/e)/\nabla T = L_{12}/\sigma$. In the classical picture, introducing a chemical potential gradient *via* doping, for example, can affect charge transport along with the temperature gradient. Most measurements of thermoelectricity in carbon nanotubes do not include an explicit chemical or doping gradient, so we can define a reference coefficient Γ_{ref} for $\nabla\mu = 0$ to mathematically consider doping effects separately.

By applying a change of variables, one can simplify the previous integral.

$$V = -\int_{\mu_L}^{\mu_R} \frac{1}{e}\,d\mu + \int_{T_L}^{T_R} \Gamma_{ref}\,dT$$
$$= \frac{1}{e}(\mu_L - \mu_R) + \int_{T_L}^{T_R} \Gamma_{ref}\,dT \qquad (3)$$

After the change of variables, T_L and T_R denote the temperatures at those respective ends of the SWNTs.

In a real circuit, a counter-voltage develops through the electrodes and wires in response to the opposite ΔT in that direction. However, for our contacts at room temperature, the Seebeck coefficient of the electrodes is negligible, so this counter-voltage is negligible. Silver has $\Gamma = 1.51\ \mu$V/K, and copper has $\Gamma = 1.83\ \mu$V/K.[25] Furthermore, SWNT−silver contacts do not exhibit rectification but rather are Ohmic since the work function of randomly oriented silver particles (4.26 eV)[25] is less than that of SWNTs (4.5 eV). The $I-V$ measurements of TWGs (Figure S1) confirm this.

The Seebeck coefficient for SWNTs, Γ_{ref}, depends on several factors, including temperature,[22,26] electronic type, alignment, void fraction,[8] and doping from preadsorbed species.[20,21,24] For SWNT macrostructures like films or fibers of mixed composition, Hewitt *et al.* have measured[22]

$$\Gamma_{ref} = aT + bT^{1/2}\exp[-(T_1/T)^{1/(1+d)}] \quad (4)$$

Hewitt *et al.* specify that $T_1 = 20$ K is a temperature scale for the carrier hopping barrier between SWNTs, and d is the dimensionality for the density of SWNT−SWNT junctions (=2 for interconnected SWNTs conducting *via* percolation). The parameters $a = -0.022\ \mu$V/K^2 and $b = 2.0\ \mu$V/K$^{1.5}$ are coefficients defining the weight of the opposing metallic and semiconducting SWNT contributions, respectively, and their values are calculated to match the temperature-dependent Seebeck data for SWNT films from Hewitt *et al.*'s experiments.

On the basis of the Seebeck coefficients for SWNTs, we can define excess voltage for TWGs as $V_{xs} = V_{out} - V_{TE}$, where V_{out} is the voltage produced by the generator and V_{TE} is the predicted thermoelectric (Seebeck) voltage based on the measured temperature gradient. Excess power can likewise be defined.

$$P_{xs} = P_{out} - P_{TE} = \frac{V_{out}^2}{R_c} - \frac{V_{TE}^2}{R_c} \quad (5)$$

R_c is the mean circuit resistance, which is approximately the internal resistance of the SWNT fiber in the low-current limit. V_{TE} is calculated according to eqs 3 and 4 to provide values of P_{xs} for SWNT fibers of varying compositions, corresponding to different values of a and b in eq 3.

$$P_{xs} = \frac{V_{out}^2}{R_c} - \frac{\left(\int_{T_L}^{T_R} \Gamma_{ref} dT\right)^2}{R_c} \quad (6)$$

EXPERIMENTAL RESULTS

TWGs can generate larger peak voltage than Seebeck predictions for a SWNT fiber of mixed electronic type. Figure 2 compares absolute peak voltage to Seebeck predictions for several possible SWNT fiber compositions, based on the parameters described above and assuming the opposite temperature is 370 K (the preheat temperature). SWNTs in the fibers

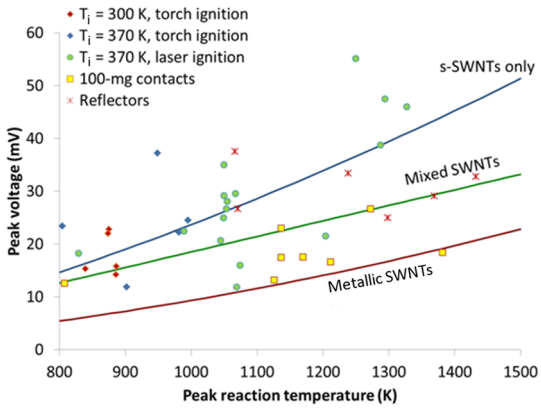

Figure 2. Peak voltage magnitude and reaction temperature for different thermopower wave generator designs. The lines indicate Seebeck effect predictions for various mixtures of metallic (m-) and s-SWNTs, assuming opposite-side $T_i = 370$ K (initial temperature). Default contact mass for other devices not specified is 200 mg; 100 mg contact TWGs and TWGs with reflectors were also preheated to 370 K and laser-ignited. The predicted V_{TE} curves were calculated using $a = -0.022\ \mu$V/K^2 and $b = 2.0\ \mu$V/K$^{1.5}$.

are not well-aligned or sorted (unlike previous MWNT arrays; see Materials and Methods), and thus their Seebeck voltage is expected to follow the trends of the two-component model of Hewitt *et al.* described above (Figure 2, middle curve).

Since $|a| < b$ in eq 3, the prediction for m-SWNTs (metallic SWNTs, with $b = 0$) is the lowest, and substantially under-predicts thermopower wave voltage. On the other hand, a fiber of only s-SWNTs (semiconducting SWNTs) would have $a = 0$ and therefore a larger magnitude Seebeck coefficient than a mixed fiber. Almost 50% of preheated, laser-ignited TWGs actually exceed the predictions for s-SWNTs, despite the unsorted nature of the source SWNTs, demonstrating that the thermopower wave can boost voltage over static thermal gradients.

On the other hand, increasing reaction temperature alone does not appear to increase voltage beyond the Seebeck prediction. The standard TWG contact mass is about 200 mg; halving that with smaller copper strips and using a minimal amount of Ag paste does tend to increase reaction temperature but without boosting voltage. Independent of other factors (*i.e.*, insulation design), the reaction temperature should be about equal across generators since they all used the same picramide (PA)/NaN_3 mix for fuel and similar amounts of fuel relative to the mass of SWNTs. Lighter contacts have smaller thermal mass, and therefore, $T_{contact}$ should increase more quickly as the reaction progresses, decreasing the flux through the contacts.

Enclosing TWGs with broad-band infrared reflectors should also decrease thermal losses due to the magnitude of radiation at high temperatures. The reflectors described in Figure 2 are stainless steel semicylinders smoothly coated with a Ag film *via* evaporation; the reflectance of Ag is >96% from 600 to 2000 nm. These TWGs used the standard 200 mg contacts, preheating,

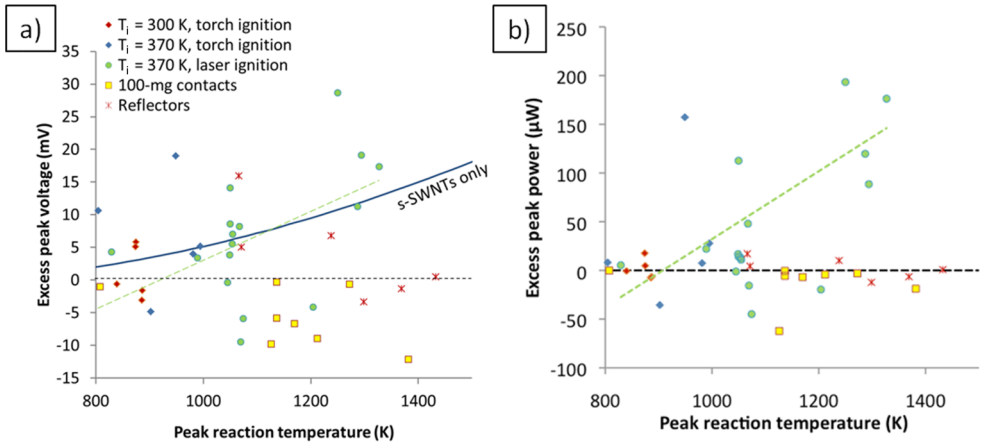

Figure 3. Electrical generation exceeding Seebeck predictions for mixed-type SWNTs, compared to reaction temperature. The dashed green lines are included to guide the eye. (a) Excess peak voltage. Of the five device designs tested, only the preheated, laser-ignited, uninsulated TWGs had an average excess $V > 0$, which increases roughly linearly with reaction temperature. The higher bound of V_{TE} for fibers composed of 100% s-SWNTs is also plotted (blue curve) for comparison. (b) Excess peak power. In laser-ignited, preheated devices, P_{xs} also increases with T, more sharply than V_{xs}.

TABLE 1. Comparing Excess Voltage Based on Two Models of SWNT Fiber Composition to Seebeck Voltage for Two Populations of Thermopower Wave Generators

	V_{xs}/V_{TE} ratio, mixed SWNT model				V_{xs}/V_{TE} ratio, s-SWNT model			
	min	max	mean	standard deviation	min	max	mean	standard deviation
$V_{xs} < 5$ mV ($N = 7$)	−44%	31%	−3%	27%	−74%	14%	−31%	32%
$V_{xs} \geq 5$ mV ($N = 9$)	26%	109%	54%	25%	−2%	68%	19%	23%

and laser ignition. Although the reflectors have a higher average peak voltage than the 100 mg contact devices (Figure 2), they still do not measurably outperform TWGs without insulation. Devices with reflectors do reach higher reaction temperatures, 1200 ± 150 K, than uninsulated TWGs, however. If only the Seebeck effect generated voltage, these higher reaction temperatures should proportionally increase peak voltage. Instead, voltages from TWGs with reflectors are not higher than those of the cooler-reacting, uninsulated TWGs, indicating that another mechanism—excess thermopower—must be at work to add to the uninsulated voltages and/or partially negate the voltages from TWGs with reflectors.

Figure 3 shows data from the experiments of Figure 2 stated in terms of V_{xs} and P_{xs} to provide a clearer picture of the trends of excess thermopower. The patterns are slightly different since the Seebeck coefficient (used to calculate V_{xs}) increases nonlinearly with temperature. The TWGs with the best design (preheated, laser ignition, 200 mg contacts) show a significant V_{xs} and P_{xs} increasing with reaction temperature and even surpassing predictions for 100% s-SWNTs (blue curve in Figure 3a). Peak power varies more than voltage because of the variable internal resistance, R_{int}, of TWGs, but P_{xs} is a significant fraction of the total peak power, as Figure 3b shows: 30−80% among TWGs with positive P_{xs} (although the lowest-power TWG generated 70% less power than the Seebeck prediction). Notably, these SWNT-based TWGs generate excess voltage like 22 nm diameter, 4 mm long, aligned arrays of MWNTs[1] despite different material properties of the SWNT fibers (length <50 μm, abundant tube−tube junctions, low alignment).

Table 1 summarizes Figure 3a in terms of the relative magnitude of excess voltage compared to Seebeck voltage. The two populations (with sample size N) correspond to those TWGs generating voltage approximately equal to or less than the Seebeck prediction (first row) and those generating significantly more (second row). The table considers only laser-ignited TWGs preheated to $T_i = 370$ K using standard contacts (mass = 200 mg) and no reflectors (green circles in Figure 3a). These statistics were calculated using two possible values of V_{TE} based on eq 4, assuming a mix of s- and m-SWNTs as described before, or the upper bound—a fiber of 100% s-SWNTs (blue curve in Figure 3a). The standard deviations are also percentages, that is, not a fraction of the mean V_{xs}/V_{TE} percentage.

The TWGs generating excess voltage produce significantly more than the population that the Seebeck effect could explain. For either model for SWNT fiber Seebeck coefficient (mixed or s-SWNTs), the means of the two populations are about two standard deviations apart. The Student's t test quantifies this difference; for the mixed SWNT model, the probability that the two populations are part of two sets with equal means is 0.07%. For the s-SWNT model, the chance is 0.5%. So even if the SWNTs in the fibers were all

semiconductors, it is most likely that one group of TWGs surpassed the Seebeck limit; indeed, all but two TWGs in that group generated more voltage than the s-SWNT upper bound (*i.e.*, ratio >0).

TWGs (excluding those with 100 mg contacts) range from R_{int} = 4 to 56 Ω (averaged over the temperature range of each reaction) with an average of 15 Ω, whereas the 100 mg devices range from 6 to 160 Ω with an average of 48 Ω. While connecting fibers to 100 mg contacts, the internal resistance may vary as much as 50% depending on the strain on the SWNT fibers. SWNT resistance is strain-sensitive, and shear stress from the contacts increases resistance. Stronger contacts would stabilize R_{int} for these generators, allowing them to utilize the higher reaction temperatures from decreased thermal conduction losses, which would increase power and efficiency.

Chemical Potential Gradient from Adsorbed Fuel. Most thermoelectric materials work with static thermal gradients, so $\Delta\mu$ does not change dynamically. However, for thermopower waves on nanostructures, μ can change during the chemical reaction. In dispersed SWNTs, for example, all atoms are at the surface of the nanotubes, so adsorbed molecules (*e.g.*, fuel) influence the electronic states of the SWNTs if their electronegativity is different from that of the SWNTs. Thus, the chemical potential term of eqs 1−3 can account for P_{xs} through different values of μ in the fuel-coated and bare regions of SWNTs.

$$P_{out} = \frac{V_{out}^2}{R_c} = \frac{1}{R_c}\left(\frac{1}{e}(\mu_L - \mu_R) + \int_{T_L}^{T_R}\Gamma_{ref}dT\right)^2 = \frac{1}{R_c}\left(\frac{1}{e^2}(\mu_L - \mu_R)^2 + \frac{2}{e}(\mu_L - \mu_R)\int_{T_L}^{T_R}\Gamma_{ref}dT\right) + \frac{1}{R_c}\left(\int_{T_L}^{T_R}\Gamma_{ref}dT\right)^2 \quad (7)$$

The second term is P_{TE}, so then chemical potential and the Seebeck coefficient define P_{xs}.

$$P_{xs} = \frac{1}{R_c}\left(\frac{1}{e^2}(\mu_L - \mu_R)^2 + \frac{2}{e}(\mu_L - \mu_R)\int_{T_L}^{T_R}\Gamma_{ref}dT\right) = \frac{1}{R_c e}(\mu_L - \mu_R)\left(\frac{1}{e}(\mu_L - \mu_R) + 2\int_{T_L}^{T_R}\Gamma_{ref}dT\right) \quad (8)$$

The $\Delta\mu$ is equivalent to the Fermi level shift, ΔE_F, and related to net changes in carrier concentration, Δn_l, by the quantum capacitance, which is distinct for m- and s-SWNTs according to their respective Fermi velocities, v_F.

$$\Delta\mu = \Delta E_F = p_m(\Delta n_{l,m} h v_{F,m}) + p_s(\Delta n_{l,s} h v_{F,s}) \quad (9)$$

Here, h is the Planck constant, and p_m and p_s are coefficients representing the fractions of m- and s-SWNTs, respectively, in unsorted fibers. These fractions are determined by the (*n*,*m*) rolling vectors of the SWNTs,

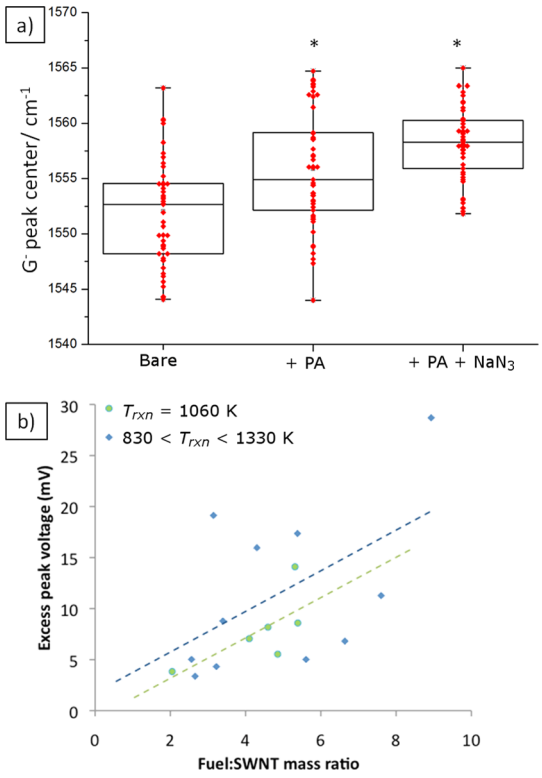

Figure 4. Doping from fuel adsorbed on SWNTs as related to excess voltage from thermopower waves. (a) Position of the Raman G⁻ peak shifts to higher wavenumbers as fuel is added to bare SWNTs. The upper and lower portions of the boxes indicate the data quartiles above and below, respectively, the average (middle line in each box) and the arms are the maxima and minima. The masses of PA and NaN_3 added were equal to that of the SWNT fiber. (b) From TWGs with (positive) excess voltage, V_{xs} increases with the proportion of fuel on the SWNTs. The green points all reacted at T = 1060 K, the mode temperature, whereas the blue points correspond to the full range of reaction temperatures measured.

so they are about 1/3 and 2/3, respectively, since the manufacturer uses a generic chemical vapor deposition process (see Materials and Methods).[27] Equation 9 is written with energy defined as for electrons; increases in electron concentration raise the Fermi level, whereas more holes lower it.

Raman spectroscopy measures doping, that is, changes in carrier concentration (normalized for SWNT cross-sectional area, so units are carriers/length), according to the shifts of peaks in the G⁻ band of SWNTs.[28] Farhat *et al.* measured individual m- and s-SWNTs doping through a top-gate electrolyte, relating the shift in G⁻ to gate voltage, V_G. One can convert these experiment-specific measurements to a general relation between G⁻ peak position and n_l knowing that, in such experiments, V_G is proportional to n_l, with contributions from geometric and quantum capacitances .

Both picramide and NaN_3 upshift the G⁻ peak, indicating p-doping. Figure 4a shows this effect based on spectra from 50 locations on a bare SWNT fiber, subsequently dosed with equal masses of PA and

NaN_3. The average peak center (middle line in each box) shifts from 1553 cm^{-1} (bare SWNTs) to 1555 cm^{-1} with the addition of picramide and then to 1558 cm^{-1} after NaN_3 addition. When comparing data sets of many individual measurements varying over similar ranges, the statistical p value test can establish the significance of differences between the sets. Its value indicates the probability that two sets originate from the same distribution, that they are not significantly different, with 0.05 generally considered the upper threshold for significance. The p values for the G^- shifts after PA and NaN_3 additions are 2×10^{-4} and 5×10^{-11}, respectively, so it is exceedingly probable that they differ significantly from the bare SWNT distribution. Control measurements with acetonitrile or water on a SWNT fiber showed no shift in the G^- peak; the fuel solvents do not contribute to doping.

Raman spectroscopy also shows, by comparing the intensities of the D and G peaks before and after reaction, that a thermopower wave does not change the defect density in a SWNT fiber (Figure S2). Either the fuel reacts without damaging the SWNTs, or a very thin outer layer of SWNTs in the fiber could be burning away, leaving the fiber mass not measurably different while exposing a new layer of undamaged SWNTs to the Raman probe. In either case, the SWNT fiber maintains its conductivity and can be refueled for further reactions.

The 5 cm^{-1} shift after PA and NaN_3 additions corresponds to Δn_l of 25 holes/μm. This change is equivalent to 10^{15} cm^{-3}, a significant doping level. The NO_2 groups of PA are strongly electron-withdrawing, consistent with the observed p-doping. As for NaN_3, the azide anion decomposes to N_2 (g) during the reaction, making its doping contributions negligible. The remaining adsorbed Na^+ ions thus p-dope the SWNTs.

The chemical potentials for bare and fueled SWNTs are thus 0.67 and 0.57 eV, respectively. Ambient atmospheric conditions will dope SWNTs to some degree, but the Fermi level of Farhat *et al.*'s SWNT at $V_G = 0$ sets the baseline for μ values. Regardless of the baseline, this difference shows that a reaction wave can create $\Delta\mu$ of 100 mV across the SWNTs, a value large enough to account for all experimental V_{xs} (maximum value 29 mV).

However, actual PA-NaN_3-SWNT devices do not reach the 100 mV upper bound of $\Delta\mu$ for several reasons. First, SWNTs in the fibers are not dispersed as individual nanotubes, so fuel will not coat all surfaces equally, leading to incomplete electron transfer to fuel molecules. Also, the reaction may not propagate along the entire fiber, leading to $\mu < 0.67$ eV behind the front. Figure 4b shows that increasing the fuel loading on the SWNTs tends to increase V_{xs}, supporting the idea that more complete reactions increase $\Delta\mu$. The correlation is stronger among TWGs with the same peak temperature during reaction, T_{rxn} (1060 K, the mode value, R^2 correlation of 0.48; compared to $R^2 =$ 0.29 for all TWGs with $V_{xs} > 0$, for which $830 < T_{rxn} <$ 1330 K). Examining data at constant T_{rxn} controls for V_{TE}, so any variations are due to differences in $\Delta\mu$. Overall, the distribution of Raman shifts (Figure 4a) indicates that SWNTs experience different doping levels, leading to variability in V_{xs}.

Voltage Polarity. Describing the evolution of thermopower wave temperature profiles over time allows one to predict, through the Seebeck effect, the shape of the voltage profile in time. In the simplest case, that of the adiabatic, steadily propagating reaction wave, during the reaction, T_R and T_L are constant, as shown by example in Figure 5a. Thus, a square, unipolar voltage pulse (Figure 5b) results from an adiabatic reaction wave according to eq 3 (assuming $\Delta\mu = 0$ between the two ends).

However, in reality, reaction waves have thermal losses from radiation, convection, and conduction and therefore will diverge from the logistic adiabatic wave temperature and voltage profiles. In particular, radiation is significant because of its fourth-order temperature dependence and the reaction temperatures exceeding 1000 K. Then the energy balance for the reacting fuel is

$$\rho C_p \frac{\partial T}{\partial t} = \chi \frac{\partial^2 T}{\partial x^2} - (\Delta H k_0 Y) e^{-E_a/RT} - \frac{\varepsilon \sigma_B S}{V}(T^4 - T_{amb}{}^4) \quad (10)$$

where t is time, x is distance, χ is thermal conductivity, ρ is density, ΔH is the enthalpy of reaction, C_p is the specific heat (mass basis), Y is the concentration of fuel (mass basis), k_0 is the Arrhenius prefactor, R is the universal gas constant, E_a is the activation energy, S/V is the exterior surface-area-to-volume ratio, ε is the emissivity, σ_B is the Stefan–Boltzmann constant, and T_{amb} is the temperature of the surroundings.

The corresponding first-order reaction kinetics equation for solid fuel (no mass diffusion) is

$$\frac{\partial Y}{\partial t} = -(k_0 Y) e^{(-E_a/RT)} \quad (11)$$

Readers interested in further details of the development of the adiabatic equations may consult ref 11. These equations can then be nondimensionalized as demonstrated in previous modeling work:[11,12] temperature $u = (R/E_a)T$, time $\tau = (-\Delta H k_0 R/C_p E_a)t$, space $\xi = x((\rho C_p/\chi)(-\Delta H k_0 R/C_p E_a))^{1/2}$, and concentration $y = (Y/\rho)$. The resulting equations are

$$\frac{\partial u}{\partial \tau} = \frac{\partial^2 u}{\partial \xi^2} + y e^{-1/u} - w(u^4 - u_{amb}{}^4) \quad (12)$$

$$\frac{\partial y}{\partial \tau} = -\beta y e^{-1/u} \quad (13)$$

with $w = (S/V)(\varepsilon\sigma\beta/\rho k_0 C_p)$ and $\beta = (C_p E_a/-\Delta HR)$; β is the inverse dimensionless adiabatic reaction temperature rise and thus is inversely related to the maximum temperature behind the reaction front.

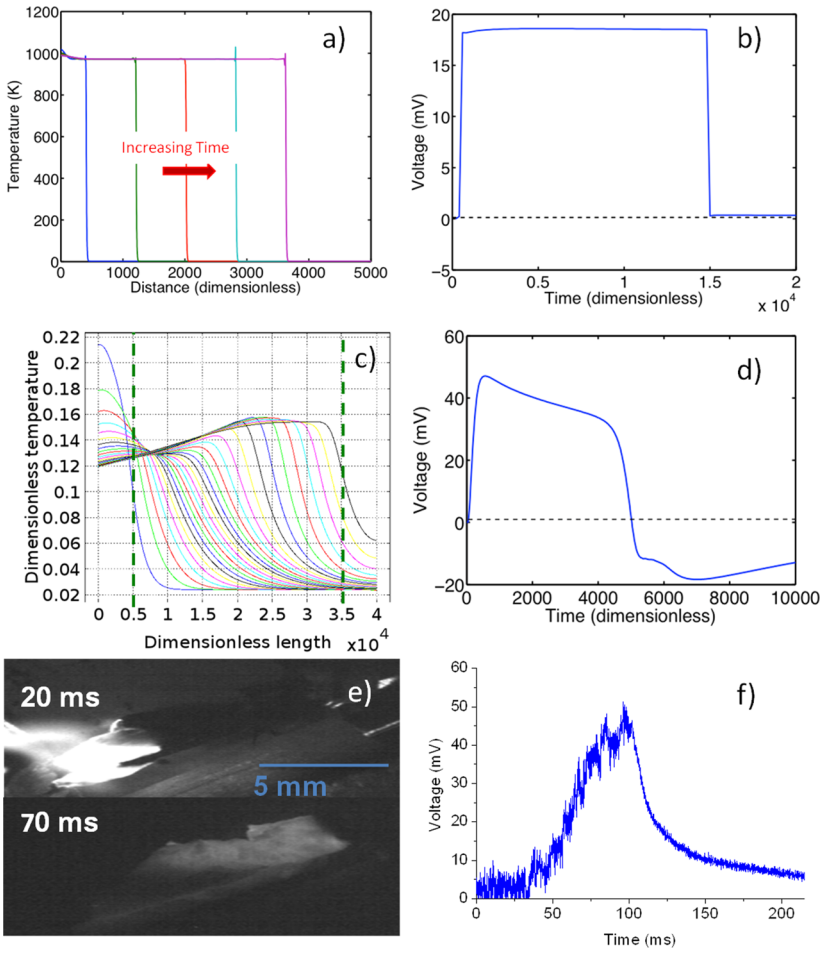

Figure 5. Theoretical predictions and experimental data for voltage polarity. (a) Simulated temperature profiles of an adiabatic reaction wave from t = 2000 to 18 000 in steps of 4000; β = 3, E_a = 24 kJ/mol. (b) Voltage profile for the wave in (a), based on contacts at 100 and 3000. (c) Simulated temperature profiles for a wave with losses from radiation and conduction losses to the contacts (t = 200 to 5600, Δt = 200); β = 8, radiation coefficient $w = 5.3 \times 10^{-5}$, and boundary conduction coefficient q = 0.34. (d) Voltage profile for wave in (c), based on contacts at 5000 and 35 000 (dashed lines). (e) Example thermopower wave images, showing cooling behind the wavefront (decreased intensity of thermionic emission). (f) Voltage measurement from wave in (e), which is unipolar despite the nonadiabatic nature of the wave.

For thermopower waves, highly thermally conductive nanoconduits with large aspect ratios accelerate the reaction wave along their lengths. As shown previously,[1,29] heat transfer between fuel layers and the conduits around which they are wrapped is not limiting, so both attain the same temperature profile moving with a velocity determined by the thermal diffusivity of the conduit. This effect can be incorporated in eq 3 by multiplying the thermal diffusion term by the ratio of conduit to fuel thermal diffusivities, α_2/α. For this case, w uses the exterior S/V for the whole SWNT fiber to avoid the complications of representing radiation within the structure.

For the SWNTs, χ decreases dramatically as T increases above room temperature, which the model considers to accurately predict thermopower wave properties. From 300 to 800 K, Pop *et al.* measured a decreasing trend somewhat steeper than $1/T$ in the thermal conductivity of a SWNT.[30] Thus, the hotter regions of the SWNTs will distribute energy internally at much lower rates (for a fixed ΔT) compared to the cooler edge of the advancing reaction wave, but the fuel in the hot zone is already reacted. By contrast, the region around the wavefront contains more unreacted fuel, driving forward and accelerating the reaction wave along with the large ΔT across the front, as previous modeling efforts have shown.[1,2,11] Thus, the characteristic χ for the system is that of the intermediate temperature of the reaction front, about 700 K.

The value of χ does not affect power output in the Seebeck theory; the power factor is $\Gamma^2\sigma$. (Both Γ and σ also depend on temperature, with functional forms included in the model that eqs 1−4 develop.) However, it can play a role for thermopower waves since reaction wave velocity increases approximately linearly with α_2. Qualitatively, faster waves produce shorter duration voltage peaks with steeper increases to peak magnitude.

Equations 12 and 13 were solved numerically using COMSOL 4.1. Using adiabatic boundary conditions and a sufficiently large initial Gaussian temperature pulse

($u = ge^{-\xi^2}/w_i + u_{amb}$) as described previously[11] (*e.g.*, $g > 0.16e^{0.37\beta}$ for $w_i = (2 \times 10^{-5})L^2$, where L is system length) ensures self-sustaining wave propagation. To match experiments, the system was initialized at 350 K with unreacted fuel ($y = 1$) everywhere. Reaction and thermal parameter values were taken from picramide (the fuel), except for thermal diffusivity (α_2/α), set by the SWNT thermal conduits as described above: C_p = 2424 J/kg/K, ρ = 1762 kg/m^3, E_a = 121 kJ/mol, k_0 (Arrhenius prefactor) = 1.6×10^7 s^{-1}, α_2/α = 25 000. Other parameters, related to radiation, are defined based on values typical of SWNT fibers used in experiments: $\varepsilon = 0.9$, $S/V = 2900$ m^{-1}.

Thermal conduction to the electrodes is another potential thermal loss mode. In thermopower wave experiments, the contacts have high interfacial surface area and are quite massive compared to the fuel-coated nanotubes (at least 50 times larger), so they act as large thermal reservoirs. Mathematically, such reservoirs can be represented as a Neumann boundary condition.

$$\frac{\alpha_2}{\alpha}\left(\frac{\partial u}{\partial \xi}\right) = q(u_{amb} - u) \qquad (14)$$

Here q is termed the thermal flux coefficient, scaling the rate of heat loss through the boundary.

Thermal losses significantly affect the wave temperature profiles. Figure 5c shows temperature profiles over time for a wave with $\beta = 8$, radiation losses ($w = 5.3 \times 10^{-5}$, derived from experimental values described above), and conduction to the contacts ($q = 0.34$), which requires $g = 7$ to initiate propagation. The velocity is about 8% of the adiabatic wave in Figure 5a, for which $\beta = 3$, $w = 0$, $q = 0$, and E_a = 24 kJ/mol (the latter specified to tune simulated temperatures to the range of those measured). The simulations of Figure 5c,d use a higher value of β than those of Figure 5a,b to highlight differences between adiabatic and nonadiabatic conditions. From the dimensional scalings, higher values of β decrease the magnitude of the reaction term relative to the other terms in the energy balance, such as the conduction and radiation thermal loss. Using $\beta = 8$ sets the system farther from adiabaticity than $\beta = 3$. The wave initiation period is visible at the left as the ignition pulse dies down and the front spreads forward. The wave then accelerates and attains the adiabatic reaction temperature ($1/\beta + u_{amb}$) at the front, while cooling by about 25% behind it (*i.e.*, at the left boundary). Voltage proportionally decreases with temperature after the peak (Figure 5d). When the right-side contact (ξ = 35 000) reaches reaction temperature, the thermal gradient reverses, creating the second V peak of opposite polarity—a bipolar voltage pulse for this realistic, nonadiabatic reaction wave.

Experimental thermopower waves share the nonadiabatic thermal characteristics of these simulations, but their voltage pulses are unipolar, in contrast to the bipolar form the Seebeck effect predicts for monotonically decreasing ΔT between the two contacts during the reaction (Figure 5d). Cooling behind the reaction front is visible as decreased thermionic emission, for example, in the excerpted images of Figure 5e. These images show a thermopower wave from picramide and NaN_3 reacting on SWNTs. However, the voltage pulse from this wave is unipolar (Figure 5f). Another important difference between these measurements and the theoretical predictions is that the maximum voltage occurs when the wave reaches the opposite contact. For the simulations (Figure 5a–d), the peak voltage occurs when the wave begins propagating at the left end of the domain, that is, when ΔT is largest. An additional voltage component from $\Delta\mu$ would be zero at the beginning of the reaction when fuel coats the whole length of the SWNTs, and then the component would grow during the reaction, offsetting the decreasing V_{TE} to minimize the negative voltage peak and increase the positive peak.

Even with significant cooling, the voltage pulse can be unipolar. Figure 6a shows the temperature measurements for the wave of Figure 5f, confirming monotonic cooling after the front passes (maximum temperature, about 1000 °C, measured at the right-side contact). However, the voltage peak is greater than 50 mV and unipolar (Figure 6b). This experiment used 0.53 mg each of picramide and NaN_3 deposited on a SWNT fiber (0.118 mg, 12 mm long), and the internal resistance of the generator was 8 Ω after attachment to electrodes. The temperature may be higher in the middle of the SWNTs since that region is farthest from the heat sink effects of the contacts. However, this temperature does not affect V_{TE}, which is the Seebeck potential difference between the left and right contacts, as eq 3 explains. The temperature and chemical potential at each contact determines its (electrical) potential. Seebeck voltage (V_{TE}) is only nonzero where there is a difference of Seebeck coefficients (*i.e.*, of materials). A middle temperature peak would have SWNTs on either side, and therefore, any increased potentials would cancel each other.

Figure 6b compares the measured voltage to two different models based on the temperatures in Figure 6a. (The pyrometers record more slowly than the oscilloscope, hence the discrete points of the predicted voltage curves.) The Seebeck coefficient for mixed SWNTs from Hewitt *et al.*, Γ_{ref}, predicts the curve denoted V_{TE}, lower than the peak voltage by about 30 mV. Moreover, it predicts a bipolar pulse with a negative peak of almost −10 mV.

A dynamic model of thermopower wave voltage includes differential doping effects from fuel through the rate of change of chemical potential, which eq 15

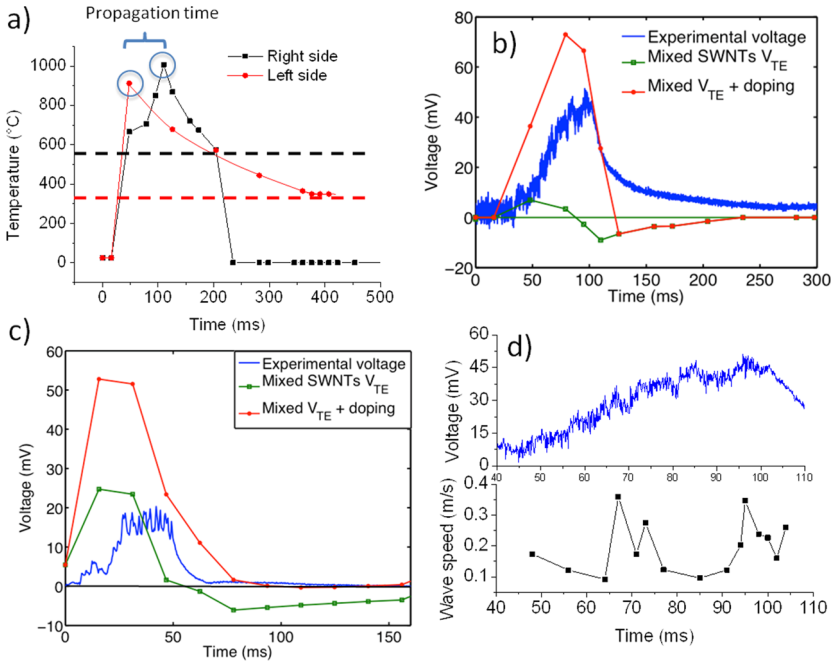

Figure 6. Synchronized voltage, temperature, and velocity measurements of thermopower waves. (a) Temperature measurements of wave in Figure 5e,f. The two pyrometers have different spectral ranges, so their lower measurement bounds (indicated by the dashed lines) differ. (b) Voltage for wave in (a), with predictions based on measured temperatures using models of thermoelectricity in SWNTs, with and without additional doping contributions. (c) Voltage profile for a different wave (temperature measurements in Supporting Information, Figure S3) with a smaller magnitude voltage peak, compared to the same thermoelectric models used to predict the green and orange voltage profiles in (b). (d) Speed of wave in (a) compared to voltage during propagation time.

develops in analogy to eq 9.

$$\frac{\partial \mu}{\partial t} = \frac{\partial E_F}{\partial t} = p_m\left(\frac{\partial n_{l,m}}{\partial t} h v_{F,m}\right) + p_s\left(\frac{\partial n_{l,s}}{\partial t} h v_{F,s}\right) \quad (15)$$

Only carrier concentration is not constant, changing with the desorption/reaction rate of the fuel, a zero-order, temperature-activated process.[31] The rate of change of carrier concentration is therefore equal for m- and s-SWNTs since the fuel binds equally to them.

$$\frac{\partial n_l}{\partial t} = \pm m k_d e^{-\Delta H_d/(RT)} \quad (16)$$

Here, m is the number of electrons donated per molecule desorbed (on the order of 1), k_d is the desorption rate constant, and ΔH_d is the enthalpy of desorption binding the fuel to the SWNTs. The sign of the rate is positive for p-doping fuels (such as picramide). Combining eqs 9 and 16 with 7 yields an explicit definition of thermopower in terms of molecular properties: the Seebeck coefficient, doping values, and fuel adsorption properties.

$$\begin{aligned} P_{out} &= \frac{1}{R_c}\left[\frac{h}{e}(p_m v_{F,m} + p_s v_{F,s})(n_{l,L} - n_{l,0,L} + \mu_{0,L} - n_{l,R} + n_{l,0,R} - \mu_{0,R}) + V_{TE}\right]^2 \\ &= \frac{1}{R_c}\left[\frac{h}{e}(p_m v_{F,m} + p_s v_{F,s})\left(\int_{t_0}^{t} \pm m k_d e^{-\Delta H_d/(RT_L)} dt - n_{l,0,L} + \mu_{0,L} - \int_{t_0}^{t} \pm m k_d e^{-\Delta H_d/(RT_R)} dt + n_{l,0,R} - \mu_{0,R}\right) + V_{TE}\right]^2 \\ &= \frac{1}{R_c}\left[\frac{h}{e}(p_m v_{F,m} + p_s v_{F,s})\left(\mu_{0,L} - \mu_{0,R} \pm m k_d \int e^{-\Delta H_d/(RT_L)} - e^{-\Delta H_d/(RT_R)} dt\right) + \int_{T_L}^{T_R} \Gamma_{ref} dT\right]^2 \end{aligned} \quad (17)$$

Here t_0 is the initial time, $n_{l,0}$ is initial carrier density, and μ_0 is initial chemical potential. The last simplification assumes that m, k_d, and ΔH_d are uniform across the SWNTs, that is, uniform fuel adsorption and electron transfer properties.

Using eqs 15 and 16 to calculate μ_L, μ_R, and V_{out} over time, the full form of eq 3 better describes thermopower wave voltage, as shown in the doping models of Figure 6b,c. (The temperature profiles corresponding to Figure 6c can be found in Figure S3.) Picramide and NaN_3 react rapidly after desorption, so k_d is set as the geometric mean of the Arrhenius prefactors of the two compounds, 2.6×10^8 1/s.[32,33] Shen *et al.* measured ΔH_d for several nitroaromatic molecules (1,3-dinitrobenzene, *m*-nitrotoluene, *p*-nitrophenol, and nitrobenzene) on CNTs to be on the order of 40 kJ/mol,[31] and Figure 6b,c uses a value of 42 ± 3 kJ/mol.

Adding the differential doping $\Delta\mu$ term thus largely or completely cancels the negative peak of the V_{TE} model. For waves with large peak voltage (>40 mV) (*e.g.*, Figure 6b), the doping model also better matches the main peak magnitude, even though Figure 6c uses a smaller value of m (0.28) according to its relatively lower fuel loading. This generator contained 0.046 mg of picramide and 0.069 mg of NaN_3 on a 0.046 mg SWNT fiber (9 mm long; internal resistance = 26 Ω). The variability in doping contributions may stem from differences in internal structure and density of junctions in the SWNT fibers, which have densities (normalized by the cross-sectional area of the fibers) ranging from 3 to 35 mg/m. Accordingly, fuel coating of SWNTs may vary, as well as the junction density parameter d. To the extent that the SWNTs are not individually dispersed within the fiber (*i.e.*, some are inside bundles), they are not accessible to fuel doping. Thus, the actual doping is likely to be less than the model prediction, bringing the theoretical curves closer to the experimental voltage pulses.

Previous discussion of the large voltages of thermopower waves focused on the wave velocities (up to 2 m/s).[1] We posited these effects as "electron [or hole] entrainment" to phenomenologically describe charge carriers caught up in and accelerated by the rapidly moving reaction front. However, Figure 6d shows no strong correlation between $|V|$ and instantaneous wave velocities measured synchronously. While the velocity fluctuates between 0.09 and 0.36 m/s, a factor of 4 difference, the amplitude of V oscillations is at most 10 mV. The V oscillations likely stem from uneven fuel coating of the SWNTs (leading to nonuniform reaction rates), as well as from the inherent velocity oscillations of the reaction wave, as a previous study explored.[11]

CONCLUSIONS

Thermopower wave generators produce power as much as 120% in excess of the predictions of the Seebeck effect for 100% s-SWNT fibers. The excess thermopower is likely larger than this bound since the SWNT fibers in these experiments also contain metallic SWNTs, decreasing their Seebeck coefficients. Excess voltage and power increase with temperature but also with the proportion of fuel loaded on the SWNTs. Raman analysis of fueled SWNTs shows an upshift in the G^- peak of 5 cm^{-1}, equivalent to a differential doping of 25 holes/μm, which can create a chemical potential difference of up to 100 mV relative to the bare SWNTs behind the wavefront. Fundamentally, since chemical potential differences also drive carrier motion, differential doping between the reacted (hot) and unreacted (cool) ends of the SWNTs can explain excess voltage.

Simulations show that nonadiabatic waves should produce bipolar voltage pulses. However, measured voltage pulses are often unipolar, despite significant thermal losses. The chemical potential difference is approximately unipolar in time and thus can cancel the opposite potential of the secondary voltage peak, yielding a unipolar pulse. This work opens a new design space for thermoelectric devices, through intentional design of doping. If the thermoelectric conduits are nanostructures, the adsorbed fuel creating the thermal gradient can also dynamically increase the potential gradient and output voltage of the generator during its reaction.

MATERIALS AND METHODS

To prepare TWGs, we used SWNT fibers from KH Chemicals (South Korea), (length = 5−20 mm; width = 0.5−2 mm). These commercially available fibers are longer than our custom-grown aligned MWNT arrays, in which individual nanotubes were 2−4 mm, simplifying generator construction. The electrical properties of the SWNT fibers vary less than MWNTs due to their more consistent growth conditions. They are acid-treated to remove leftover metal catalyst from the chemical vapor deposition synthesis process, and each fiber contains millions of SWNTs (individuals or small bundles) with diameters of 1.0−1.3 nm and lengths of 5−50 μm, as reported by the manufacturer and confirmed by Raman spectroscopy and electron microscopy. Moreover, the SWNT fibers are more porous than the other main commercially available one-dimensional SWNT macrostructures, yarns in which SWNTs are spun to create an ordered cable meters long. Therefore, fuel molecules can adsorb to more of the fibers' internal surface area, enhancing the chemical potential doping effects that are the subject of this study.

Picramide and sodium azide together form a good fuel mixture for thermopower waves. PA provides large ΔH for high temperature, whereas NaN_3 lowers overall E_a, increasing reliability of ignition. The fuel compounds physically adsorb to the SWNTs after deposition from their respective solutions (PA, 20 g/L in acetonitrile; NaN_3, 20 or 50 g/L in water). The solvents evaporate for 1 and 4 h, respectively, after addition of each solution. The masses of PA and of NaN_3 should each be at least equal to the mass of SWNTs for successful reaction.

Ignition System. Thermopower waves were ignited with a 350 mW fiber-optic laser emitting 100 ms pulses (to match the time scale of the waves) at 785 nm, an absorption maximum of SWNTs, thereby decreasing the laser output power needed. A series of lenses and mirrors focused the laser spot to <1 mm^2; laser power at the sample is 300 mW. The minimum pulse intensity for ignition is 0.38 W/mm^2, corresponding to pulse energy of 30 mJ. A small electrical resistance heater (coated with silicone to prevent electrical contact with the TWGs) controlled initial temperature. Preheating the whole TWG to 50−80 °C (as measured by type K thermocouple) successfully ignited waves >90% of the time, but with initial temperature of 25 °C, waves ignite <5% of the time. Therefore, some preheating is needed. Without a reaction wave, the voltage changes <3 mV.

Instruments. A digital oscilloscope (Yokogawa DL 1735E or 2000) measures voltage, and a high-speed camera records the wave propagation at 1000−4000 frames/s (Canadian Photonic Laboratories, CPL-MS70KS2B90) with a Nikon, AF Micro-NIKKOR 60 mm f/2.8D macro lens for sample magnification. Two pyrometers (Raytek MM1MH and Omega OS4000) measure temperature at the left and right ends, respectively, of each SWNT fiber. The Raytek measures spectral response at 1 μm with a semiconductor photodetector and calculates temperature assuming (emissivity-adjusted) blackbody emission (accuracy = ±0.3% + 1 K; range = 540 °C < T < 3000 °C). The Omega uses an InGaAs photodetector (spectral response = 1.2 to 2.6 μm, accuracy = ±1%, 350 °C < T < 1500 °C). Since carbon nanotubes are nearly blackbody emitters with little wavelength

dependence in their emission, this approach is valid. Moreover, we measured the temperature-dependent emissivity of these SWNT fibers by comparing temperatures recorded by a type K thermocouple and a thermal camera (FLIR 7650). The ε ranges from 0.82 to ~1 from ambient to reaction temperatures and is ≥0.98 above 800 K, so it is nearly constant for the pyrometers.

Simulations. COMSOL employs adaptive time-stepping to improve calculation stability. We confirmed convergence by comparing results at several spatial mesh sizes. Figure 5a–d was created with mesh size $\Delta\xi = 1$, and Figure S4 shows temperature profiles for three other mesh sizes with $\beta = 4$ and $w = 2.7 \times 10^{-5}$. Wave shape and speed do not change over $0.5 < \Delta\xi < 4$. The simulation initiation parameters were g (initial Gaussian amplitude) = 2.1 and w_i (Gaussian peak width parameter) = 5000.

Conflict of Interest: The authors declare no competing financial interest.

Acknowledgment. The Air Force Office of Scientific Research (AFOSR) supported this work through Grant FA9550-09-1-0700. Additionally, the MIT Energy Initiative and Undergraduate Research Opportunities Program supported J.M.F. and M.P.W. J.T.A. would like to thank T. McNicholas and K. Tvrdy for helpful discussions. F.S. and S.S. thank TUBITAK for 2211 and 2214-Research fellowship program and the METU-DPT-OYP program on the behalf of Yuzuncu Yil University. B.S. thanks Universitat Ramon Llull for support.

Supporting Information Available: Calculation of predicted Seebeck voltage for ZnO; resistance measurements confirming Ohmic behavior of SWNTs in thermopower wave generators; Raman D/G ratios indicating very low damage to SWNT fibers by thermopower waves; temperature measurements for Figure 6c; convergence tests for COMSOL simulations. This material is available free of charge *via* the Internet at http://pubs.acs.org.

REFERENCES AND NOTES

1. Choi, W.; Hong, S.; Abrahamson, J. T.; Han, J.-H.; Song, C.; Nair, N.; Baik, S.; Strano, M. S. Chemically Driven Carbon Nanotube-Guided Thermopower Waves. *Nat. Mater.* **2010**, *9*, 423–429.
2. Choi, W.; Abrahamson, J. T.; Strano, J. M.; Strano, M. S. Carbon Nanotube-Guided Thermopower Waves. *Mater. Today* **2010**, *13*, 22–33.
3. Pech, D.; Brunet, M.; Durou, H.; Huang, P.; Mochalin, V.; Gogotsi, Y.; Taberna, P.-L.; Simon, P. Ultrahigh-Power Micrometre-Sized Supercapacitors Based on Onion-like Carbon. *Nat. Nanotechnol.* **2010**, *5*, 651–654.
4. Kang, B.; Ceder, G. Battery Materials for Ultrafast Charging and Discharging. *Nature* **2009**, *458*, 190–193.
5. El-Kady, M. F.; Strong, V.; Dubin, S.; Kaner, R. B. Laser Scribing of High-Performance and Flexible Graphene-Based Electrochemical Capacitors. *Science* **2012**, *335*, 1326–1330.
6. Walia, S.; Balendhran, S.; Yi, P.; Yao, D.; Zhuiykov, S.; Pannirselvam, M.; Weber, R.; Strano, M. S.; Bhaskaran, M.; Sriram, S.; *et al.* MnO_2-Based Thermopower Wave Sources with Exceptionally Large Output Voltages. *J. Phys. Chem. C* **2013**, *117*, 9137–9142.
7. Hong, S.; Kim, W.; Jeon, S.-J.; Lim, S. C.; Lee, H.-J.; Hyun, S.; Lee, Y. H.; Baik, S. Enhanced Electrical Potential of Thermoelectric Power Waves by Sb_2Te_3-Coated Multiwalled Carbon Nanotube Arrays. *J. Phys. Chem. C* **2013**, *117*, 913–917.
8. Baxendale, M.; Lim, K.; Amaratunga, G. Thermoelectric Power of Aligned and Randomly Oriented Carbon Nanotubes. *Phys. Rev. B* **2000**, *61*, 12705–12708.
9. Walia, S.; Weber, R.; Latham, K.; Petersen, P.; Abrahamson, J. T.; Strano, M. S.; Kalantar-zadeh, K. Oscillatory Thermopower Waves Based on Bi_2Te_3 Films. *Adv. Funct. Mater.* **2011**, *21*, 2072–2079.
10. Walia, S.; Weber, R.; Balendhran, S.; Yao, D.; Abrahamson, J. T.; Zhuiykov, S.; Bhaskaran, M.; Sriram, S.; Strano, M. S.; Kalantar-zadeh, K. ZnO Based Thermopower Wave Sources. *Chem. Commun.* **2012**, *48*, 7462–7464.
11. Abrahamson, J. T.; Choi, W.; Schonenbach, N. S.; Park, J.; Han, J.-H.; Walsh, M. P.; Kalantar-zadeh, K.; Strano, M. S. Wave Front Velocity Oscillations of Carbon Nanotube-Guided Thermopower Waves: Nanoscale Alternating Current Sources. *ACS Nano* **2011**, *5*, 367–375.
12. Abrahamson, J. T.; Strano, M. S. An Analytical Solution to Coupled Chemical Reaction and Thermally Diffusing Systems: Applicability to Self-Propagating Thermopower Waves. *J. Phys. Chem. Lett.* **2010**, *1*, 3514–3519.
13. Weber, R. O.; Mercer, G. N.; Sidhu, H. S.; Gray, B. F. Combustion Waves for Gases (Le=1) and Solids (L->Infinity). *Proc. R. Soc. London, Ser. A* **1997**, *453*, 1105–1118.
14. Yu, C. H.; Shi, L.; Yao, Z.; Li, D. Y.; Majumdar, A. Thermal Conductance and Thermopower of an Individual Single-Wall Carbon Nanotube. *Nano Lett.* **2005**, *5*, 1842–1846.
15. Scarola, V. W.; Mahan, G. D. Phonon Drag Effect in Single-Walled Carbon Nanotubes. *Phys. Rev. B* **2002**, *66*, 205405.
16. Vavro, J.; Llaguno, M. C.; Fischer, J. E.; Ramesh, S.; Saini, R. K.; Ericson, L. M.; Davis, V. A.; Hauge, R. H.; Pasquali, M.; Smalley, R. E. Thermoelectric Power of p-Doped Single-Wall Carbon Nanotubes and the Role of Phonon Drag. *Phys. Rev. Lett.* **2003**, *90*, 065503.
17. Tsaousidou, M. Theory of Phonon-Drag Thermopower of Extrinsic Semiconducting Single-Wall Carbon Nanotubes and Comparison with Previous Experimental Data. *Phys. Rev. B* **2010**, *81*, 235425.
18. Pop, E.; Mann, D.; Cao, J.; Wang, Q.; Goodson, K.; Dai, H. J. Negative Differential Conductance and Hot Phonons in Suspended Nanotube Molecular Wires. *Phys. Rev. Lett.* **2005**, *95*, 155505–155508.
19. Hone, J.; Ellwood, I.; Muno, M.; Mizel, A.; Cohen, M. L.; Zettl, A.; Rinzler, A. G.; Smalley, R. E. Thermoelectric Power of Single-Walled Carbon Nanotubes. *Phys. Rev. Lett.* **1998**, *80*, 1042–1045.
20. Sumanasekera, G. U.; Adu, C. K. W.; Fang, S.; Eklund, P. C. Effects of Gas Adsorption and Collisions on Electrical Transport in Single-Walled Carbon Nanotubes. *Phys. Rev. Lett.* **2000**, *85*, 1096–1099.
21. Sumanasekera, G. U.; Pradhan, B. K.; Romero, H. E.; Adu, K. W.; Eklund, P. C. Giant Thermopower Effects from Molecular Physisorption on Carbon Nanotubes. *Phys. Rev. Lett.* **2002**, *89*, 166801.
22. Hewitt, C. A.; Kaiser, A. B.; Roth, S.; Craps, M.; Czerw, R.; Carroll, D. L. Varying the Concentration of Single Walled Carbon Nanotubes in Thin Film Polymer Composites, and Its Effect on Thermoelectric Power. *Appl. Phys. Lett.* **2011**, *98*, 183110–183113.
23. Zhang, Z. M. *Nano/Microscale Heat Transfer*; McGraw-Hill: New York, 2007; p 479.
24. Bradley, K.; Jhi, S.-H.; Collins, P.; Hone, J.; Cohen, M.; Louie, S.; Zettl, A. Is the Intrinsic Thermoelectric Power of Carbon Nanotubes Positive? *Phys. Rev. Lett.* **2000**, *85*, 4361–4364.
25. Lide, D. R. *CRC Handbook of Chemistry and Physics*, 92nd ed.; CRC Press: Boca Raton, FL, 2012.
26. Zhang, H. L.; Li, J. F.; Zhang, B. P.; Yao, K. F.; Liu, W. S.; Wang, H. Electrical and Thermal Properties of Carbon Nanotube Bulk Materials: Experimental Studies for the 328–958 K Temperature Range. *Phys. Rev. B* **2007**, *75*, 205407–205415.
27. Dai, H. Carbon Nanotubes: Synthesis, Integration, and Properties. *Acc. Chem. Res.* **2002**, *35*, 1035–1044.
28. Farhat, H.; Son, H.; Samsonidze, G.; Reich, S.; Dresselhaus, M.; Kong, J. Phonon Softening in Individual Metallic Carbon Nanotubes Due to the Kohn Anomaly. *Phys. Rev. Lett.* **2007**, *99*, 145506.
29. Abrahamson, J. T.; Nair, N.; Strano, M. S. Modelling the Increase in Anisotropic Reaction Rates in Metal Nanoparticle Oxidation Using Carbon Nanotubes as Thermal Conduits. *Nanotechnology* **2008**, *19*, 195701–195708.
30. Pop, E.; Mann, D.; Wang, Q.; Goodson, K.; Dai, H. J. Thermal Conductance of an Individual Single-Wall Carbon Nanotube above Room Temperature. *Nano Lett.* **2006**, *6*, 96–100.
31. Shen, X.-E.; Shan, X.-Q.; Dong, D.-M.; Hua, X.-Y.; Owens, G. Kinetics and Thermodynamics of Sorption of Nitroaromatic Compounds to As-Grown and Oxidized Multiwalled Carbon Nanotubes. *J. Colloid Interface Sci.* **2009**, *330*, 1–8.

32. Mohan, V. K.; Verneker, V. R. P. Role of Crystal Imperfections in Thermal-Decomposition of Sodium Azide. *J. Phys. Chem.* **1976**, *80*, 119–122.
33. Maksimov, Y. Y.; Kogut, E. N. The Relation between the Uni- and Bi-molecular Components in the Thermal Decomposition of Liquid Aromatic Nitro-Compounds. *Russ. J. Phys. Chem.* **1978**, *52*, 805–808.